Three-Dimensional Model for Determining Inhomogeneous Thermal Dosage in a Liver Tumor During Arterial Embolization Hyperthermia Incorporating Magnetic Nanoparticles

Ruizhi Xu[1], Hui Yu[2], Yu Zhang[1], Ming Ma[1], Zhongping Chen[1], Changling Wang[1], Gaojun Teng[2], Jun Ma[3], Xinchen Sun[3], and Ning Gu[1]

[1]Jiangsu Laboratory for Biomaterials and Devices, State Key Laboratory of BioElectronics, School of Biological Science and Medical Engineering, Southeast University, Nanjing 210096, China
[2]Department of Radiology, Zhongda Hospital, Southeast University, Nanjing 210019, China
[3]Tumor Center of Zhongda Hospital, Southeast University, Nanjing 210019, China

Hyperthermia treatment incorporating magnetic nanoparticles (MNPs) is a hopeful therapy for cancers. Acquiring information about the MNPs' deposition in tumor tissues and modeling magnetic heating *in vivo* are essential for successful treatment. In this paper, we discuss the inhomogeneous heat generation by MNPs distributed heterogeneously in a liver tumor during arterial embolization hyperthermia (AEH) treatments. In order to more accurately simulate the temperature elevation for an AEH treatment plan, we conducted the following experiments. First, we detected the distribution of magnetic field intensity in the aperture of a ferrite-core applicator. We found that attenuation of the magnetic field focuses mainly on the vertical distance of the aperture, which makes MNPs in tissues have different power loss along the lognitudinal axis. Second, we prepared 20 nm monodisperse lipiodol-soluble MNPs and injected super-selectively through the micro-catheter into the arteries of a rabbit with a VX-2 liver tumor. By histological cuts of the investigated specimen, as well as computed tomography (CT), we found MNPs mainly concentrated on the tumor periphery. Last, from the experimental information, we established a new model for simulating the increasing temperature in the liver tumor based on our inhomogeneous interior-heat-source analysis (IIA). We also compared the simulated results with the two types of homogeneous models. The results showed that IIA gives significantly different results from those for a homogeneous model and thus is preferable when an accurate treatment plan is required during AEH.

Index Terms—**Arterial embolization hyperthermia, magnetic nanoparticles, mathematical modeling, specific absorption.**

I. Introduction

ARTERIAL embolization hyperthermia (AEH) incorporating magnetic nanoparticles (MNPs) is a new form of local hyperthermia therapy for liver cancer. It consists of arterially embolizing liver tumors with MNPs that generate heating on exposure to an alternating magnetic field [1]–[7]. It is also one of the therapeutic methods of magnetic fluid hyperthermia (MFH) [8]–[10]. Recently, MFH has been clinically tested to treat prostate cancer [11] and glioblastoma multiforme [12] in human patients.

Diagnosis and treatment relative to hepatocellular carcinoma (HCC) are challenging problems in the world. Hepatic tumors appear to derive virtually all their blood supply from the hepatic arterial system, as compared with normal hepatic parenchyma which derives most of its blood supply from the portal venous system [13]–[16]. Selective targeting of the liver tumor is the principle on which selective internal radiation therapy (SIRT) and hepatic arterial chemotherapy (HAC) have successfully targeted liver tumors with radiation and chemotherapy respectively [17]–[20]. The AEH is based on selective arterial embolization of liver tumors through the lipiodol containing magnetic particles. On one hand, it can cut off the blood supply from the hepatic arterial system to tumors; on the other hand, with the external ac magnetic field it can heat up local tumor tissue through hyperthermia. This new method could be applied to clinical therapy relative to HCC and will have a promising future.

Tumor hyperthermia requires accurate calculation and description of the temperature distribution produced from MNPs in the tissue before it is applied in clinical trial. The temperature distribution is of great importance in determining how successful the treatment is. The vast majority of thermal dosimetry for hyperthermia has been performed using invasive temperature probes such as manganin-constantan thermocouples [21] and optic fibers [11], [12] to sample a small number of points. Thermal dosimetry using invasive thermometry is an absolute necessity to determine the temperature distributions achieved. Besides the problems with the extremely limited information about highly inhomogeneous thermal dose distributions, this invasive thermometry is a major clinical problem in the acceptance of hyperthermia. In local hyperthermia, 3-D guidance of the temperature distribution is essential, making local hyperthermia highly invasive. There are a number of noninvasive approaches under investigation which can quantify more complete 2-D and 3-D temperature distributions. These techniques involve infrared thermography, computerized axial tomography, ultrasound time-of-flight tomography techniques, electrical impedance tomography, microwave tomography, magnetic resonance imaging, and microwave radiometry. Unfortunately, 3-D noninvasive thermometry for control of hyperthermia systems is beyond the present capability of imaging systems. Magnetic resonance imaging (MRI) may provide guidance for thermotherapy applications and become a matter of importance for hyperthermia applications in the future. But at present, clinical hyperthermia has to rely on invasive thermometry [22].

Manuscript received September 22, 2008; revised November 10, 2008 and February 27, 2009. Current version published July 22, 2009. Corresponding author: N. Gu (e-mail: gunning@seu.edu.cn).

Color versions of one or more of the figures in this paper are available online at http://ieeexplore.ieee.org.

Digital Object Identifier 10.1109/TMAG.2009.2019128

Because of limited thermometry, knowledge about the temperature distributions achieved can only be obtained by hyperthermia treatment planning (HTP). HTP is a two-step process. First, the absorbed power distribution should be calculated. Second, the temperature distribution has to be computed [22]. In AEH incorporating MNPs, the nanopartilcles deposition *in vivo* and spatial power loss under external ac magnetic field determine the thermal dose in tumor tissues.

Previous studies of the heat generation analysis on internal sources have either concentrated on the cases where the magnetic field are distributed homogeneously throughout the tumor volume [23] or the micro/nanoparticles are distributed uniformly throughout the tumor tissues [7], [24] or both [25]–[27]. In AEH with MNPs, the attenuation of external ac magnetic field exists in the patient-accommodable treatment aperture. This has been detected in the couple-loops [28] and single-loop ferrite-core applicator [7], respectively. Since the inhomogeneous magnetic field makes MNPs in tissues as thermal seeds have different power loss due to spatial positions, heat deposition analysis taking account the effect of the heterogeneous magnetic field intensity may make the HTP more accurate. The phenomena have been observed that the injected particles are not uniformly distributed in the whole tumor volume in animal experiments during AEH with microspheres [5], [6], and in human patients who have received selective internal radiation therapy using radioactive microspheres for liver cancer [29], [30]. The simplifying assumption that particles are homogeneously distributed within the volume of the tumor shell is not sufficient. A more accurate representation may take into account the heterogeneous nature of the MNPs distribution incorporating inhomogeneous magnetic field.

In the ferrite-core applicator, the combination of field intensity with frequency has limitation and is low for the generation of any substantial eddy currents. The calculation of specific absorption rate (SAR) of MNPs is different from that of tissues generated by microwave, RF of ultrasound. The SAR value of MNPs depends on the microstructure and sizes of particles and the intensity and frequency of external alternating current magnetic field. We detected it by the initial temperature transient via fiber optic temperature sensor (FOTS) in the MNPs-gelled model, which represented the magnetic field distribution in the aperture.

The radiological technique of MRI [5] and micro-tomography [31] were evaluated as a potential tool for noninvasively and prospectively determining the concentration and distribution of particles within the hepatic tumor. We prepared 20 nm mono-dispersed MNPs and dissolved them homogeneously into the lipiodol. For the lipiodol highly absorbs X-rays, we used nondestructive computed tomography (CT) for analysis of the distribution of MNPs. We also identified the overall distribution of MNPs in the liver tumor by histological cuts of the investigated specimen. The result shows that the MNPs are concentrated in the tumor periphery.

Since the two heterogeneous factors are the essence of AEH on liver tumor, the analysis for three-dimensional (3-D) heat generation distribution in the tissue are required. At present, no model has simulated the temperature increase during AEH considering the two essential factors simultaneity. We therefore established a newly simplified model for simulating the temperature elevation in the tumor tissue. The theoretical model showed some characteristic of temperature elevation and thermal distribution in liver tumors during AEH treatment. The simulated results may explain some phenomena of temperature detecting in present rabbit VX-2 experiments [2]–[4], [6]. We also compared the simulated results with the two types of homogeneous models at present to show the significant difference. We believe that the inhomogeneous interior-heat-source analysis (IIA) would help provide accurate and reliable simulation results and a theoretical and technical basis for controlling temperature during AEH therapy.

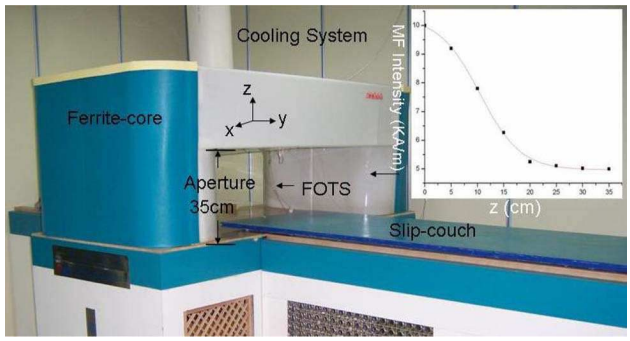

Fig. 1. The ferrite-core applicator operating system during AEH treatment and the curve of detection of ac magnetic field intensity along the vertical distance in the treatment aperture.

II. Methods

A. Ferrite-Core Applicator

We set up the AEH therapy system for clinical investigations at Jiangsu Laboratory for Biomaterials (Fig. 1). The thermal therapy device consists basically of a resonant circuit at a ferrite yoke that generates an alternating magnetic field between two pole-shoes above and underneath the treatment aperture. The aperture (vertical distance 350 mm, length 300 mm, and width 200 mm) was developed specifically for accommodating patients. A slip-couch allows a patient to be moved into and through the aperture, so that any part of the body can be exposed by the magnetic field. The device is operated at a frequency of 80 kHz. The field strength can be adjusted from 0 to 10 kA/m.

We detected the physical parameters of magnetic field distribution in the aperture. We found the attenuation of magnetic intensity focused on the longitudinal z-direction, while slighter on transversal x- and y-axis at the same level. The tumor tissue in the treatment aperture has the volume in which magnetic intensity distributed heterogeneously. The heating effect depends heavily on the properties and concentration of the MNPs, heating area of tissue, and the frequency and strength of the external alternating magnetic field. From the bottom to top, the magnetic strength decreased 50%. If more accurate clinically HTP required, the heat source analysis considering the effect of inhomogeneous magnetic field would provide more precise results compared with some present models [23]–[27].

B. MNPs in Rabbit VX-2 Liver Tumor

We synthesized monodisperse MNPs by thermal decomposition method [31]–[35]. We used the lipiodol as embolic property and carrier medium of MNPs. The model of rabbit VX-2 liver tumor was established by Department of Radiology, Zhongda Hospital. After embolization, we observed the cross section of a VX-2 carcinoma excised from a rabbit. Some MNPs had been assembled for high concentration, which made microscopic ex-

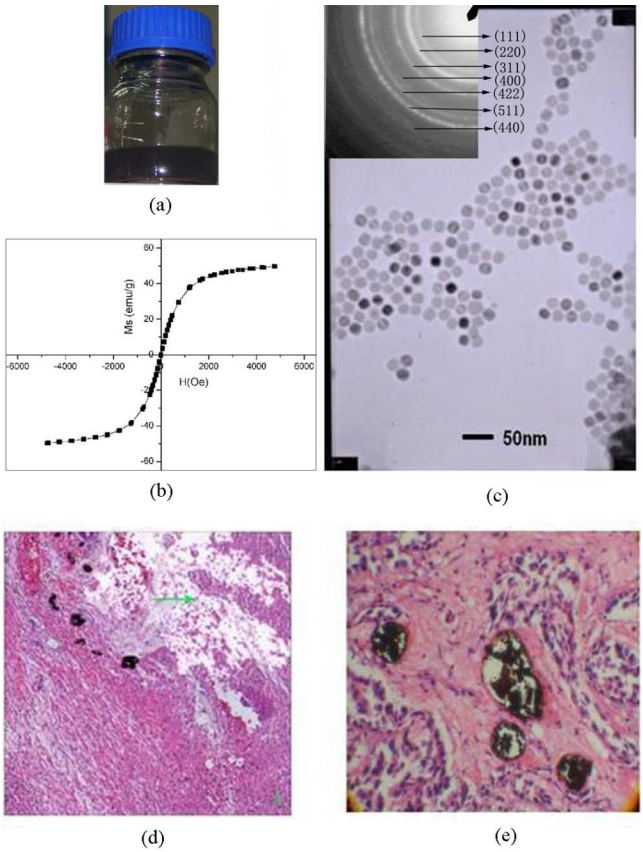

Fig. 2. The preparation of MNPs with 20 nm diameters dispersed in the lipiodol (a). Magnetic property of the nanoparticles was shown in (b), indicating superparamagnetic behavior at room temperature, with no hysteresis and perfect Langevin behavior. The respective (111), (220), (311), (400), (422), (511), and (440) hkl planes of iron oxide nanoparticles were indexed in figure (c). The local information about the overall distribution of MNPs determined by histological cuts of a VX-2 carcinoma excised from a rabbit, showing particles deposited within the vascular periphery and adjacent necrotic region devoid of particles (d). MNPs were mainly found in vessels supplying tumor cells (e).

amination easy. Particles are mainly found in the vessels supplying tumor cells and deposited within the vascular periphery and adjacent necrotic region devoid of MNPs (Fig. 2).

Histological examinations offer a versatile method and the possibility of getting quantitative information about the magnetic particle concentration with a spatial resolution in the micrometer range and can be further extended to the nanometer range by using electron microscopy. But due to its destructive nature, Brunke *et al.* [36] studied the imaging with γ-rays and X-rays to examine the distribution of MNPs *in vivo* during the application of the drug. The iron-based MNPs serve as a contrast agent that have higher X-ray attenuation coefficients compared to biological tissue and additionally X-ray radioscopy generally provide much higher spatial resolution compared to γ-imaging, which makes micro-CT a potential tool for a 3-D analysis of the distribution of MNPs in biological applications.

We prepared MNPs oil-soluble particularly by the particle surface-coating technique. We dissolved MNPs uniformly into the lipiodol which has been clinically used as an embolic property. The lipiodol provides much higher absorption for X-rays than MNPs. Therefore, we conveniently used CT to investigate the MNPs-dispersed-lipiodol distribution in the VX-2 liver tumor. After embolization, the MNPs distribution within the liver tumor was not homogeneous. Fig. 3 clearly shows a highly

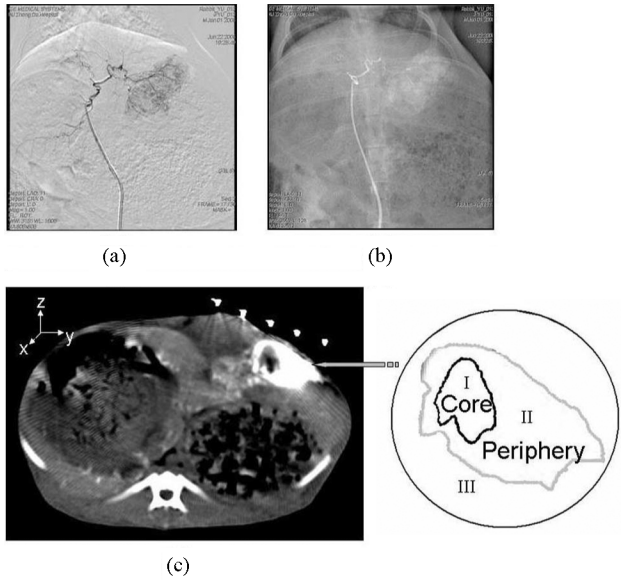

Fig. 3. The hepatic arterial system of a VX-2 carcinoma when injected with the contrast medium under X-rays before embilizaton, showing the abundant vascular accommodation of MNPs (a). After embolization, the lipiodol with MNPs replaced the X-rays contrast. MNPs were distributed homogeneously into the lipiodol which provides sufficiently high absorption for X-rays and thus the particle distribution in VX-2 carcinoma was determined by CT (c). Three independent zones were divided visibly: (I) tumor core, (II) tumor periphery, and (III) normal boundary tissue.

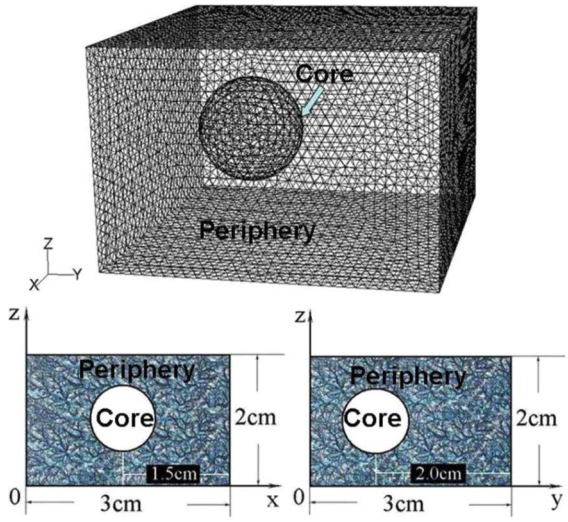

Fig. 4. The theoretical model established to show the characteristic of temperature rise during AEH treatment. The cuboid tumor tissue with vertical distance 20 mm, length 30 mm, and width 30 mm, the central sphere, as necrotic region, without MNPs distributed.

vascularized region containing large amounts of MNPs adjacent to a poorly vascularized and necrotic region with virtually no MNPs. Three independent zones were divided; tumor core without MNPs distributed, tumor periphery accommodating the lipiodol with MNPs and normal boundary tissue.

C. SAR Measurement

1) Study of SAR in Pennes' Equation: Since the two essential factors affect the magnetic heating during AEH, the analysis of inhomogeneous interior heat source in the bio-heat transfer equation is essential for computation.

The thermal models have been established such as the earliest Pennes (BHT) Model, the Chen and Holmes (CH) Model,

and the Weinbaum-Jiji and Lemons (WJL) Model. The Pennes model [37] for describing heat transfer in a tissue, originally designed for predicting temperature fields in the human forearm, has become well known as the "bio-heat transfer" equation. The CH model [38] of bio-heat transfer is obtained by replacing the single perfusion term in the Pennes model with the vascular contributions. The WJL model [39] is based on completely different vascular generations: the WJL equations apply to thermally significant small vessels and not to major supply blood vessels.

Due to its conciseness and validity, up to now, nearly all the property measurements are based on the well-known Pennes' bio-heat equation which is written as

$$\rho C\frac{\partial T}{\partial \tau} = \nabla\cdot(K\nabla T) + \omega_b C_b(T_a - T) + Q_r \tag{1}$$

where ρ is density of the tissue (kg/m^3), C is specific heat of tissue (J/kg°C), T is tissue temperature, τ is time (s), K is thermal conductivity of tissue (W/m°C), ω_b is blood perfusion rate (kg/m^3), C_b is specific heat of blood (J/kg°C), and Q_r is heat generation due to external heat source respectively (W/m^3).

Andra [25], Rosensweig [40], and Pankhurst *et al.* [41] gave the formula of heat generation by MNPs, respectively. Actually from the histological cuts and CT, MNPs spatial distribution is not homogeneous in the whole bulk of tissue region. SAR is a function of H_i and f. The value of H_i is a function of space as a consequence of the attenuation of the magnetic field. Then, we concluded that

$$Q_r = \mathrm{SAR}(x,y,z)\cdot\xi_{\mathrm{Fe}}(x,y,z) \tag{2a}$$

$$Q_r = \mathrm{SAR}(x,y,z)\cdot\xi_{\mathrm{MNP}}(x,y,z) \tag{2b}$$

where ξ_{Fe} or ξ_{NP} is the bulk of tissue unit containing the mass of the element Fe of or MNPs (g of Fe/m^3 or g of MNP/m^3).

2) Measurement of SAR: According to the equation by Ma [42]

$$\mathrm{SAR} = C\frac{\Delta T}{\Delta \tau}\frac{1}{m_{\mathrm{Fe}}} \tag{3}$$

where C is the sample-specific heat capacity which is calculated as a mass weighted mean value of magnetite and water. $\Delta T/\Delta\tau$ is the initial slope of time-dependent temperature curve. m_{Fe} is the iron content per gram of the Fe_3O_4 or γ-Fe_2O_3 suspension solution. Here, the physical parameters (H_0 and f) of ac magnetic field are taken as constants, although the actual field intensity is inhomogeneous in the aperture.

In virtue of the difficulty to detect the effect of the attenuation of external magnetic field on SAR values of MNPs in the suspension solution, we established specific SAR measurement in the MNPs-gelled composite phantom. The blood perfusion ω_b and the thermoregulation mechanisms Q_m are neglected in the *in vitro* model. The heat transfer equation is

$$\rho C\frac{\partial T}{\partial \tau} = K\left(\frac{\partial^2 T}{\partial x^2} + \frac{\partial^2 T}{\partial y^2} + \frac{\partial^2 T}{\partial z^2}\right) + Q_r \tag{4}$$

where $Q_r = \mathrm{SAR}(x,y,z)\cdot\xi_{\mathrm{Fe}}(x,y,z)$.

At the instant the device power is switched on, the conduction heat transfer in the phantom is negligible, and the partial derivative of temperature is in respect to the SAR [7], [42].

$$\left.\frac{\partial^2 T}{\partial x^2} + \frac{\partial^2 T}{\partial y^2} + \frac{\partial^2 T}{\partial z^2}\right|_{\tau=0} = 0 \tag{5a}$$

$$\left.\rho\, C\frac{\partial T}{\partial \tau}\right|_{\tau=0} = \mathrm{SAR}(x,y,z)\cdot\xi_{\mathrm{Fe}}(x,y,z). \tag{5b}$$

When in a small unit of the composite, the distribution of nanoparticles can be taken as homogenization,

$$\xi_{\mathrm{Fe}}(x,y,z) = \xi_i \tag{6a}$$

where ξ_i is a constant; therefore, the value of SAR at a spatial spot is

$$\mathrm{SAR}(x,y,z) = \rho\, C\left.\frac{\partial T}{\partial \tau}\right|_{\tau=0}/\xi_i. \tag{6b}$$

We detected the SAR values of MNPs by FOTS at some spots along the vertical distance of the aperture. From the SAR values measured at some spots measured, the function of heat generation $Q_r(z)$ can be concluded by curve fitting technique.

D. Theoretical Thermal Model

We analyzed the two essential factors in the interior-heat-source and expressed them in (6). The SAR values of MNPs are detected *in vitro* and the 3-D particles SAR distributions in tissues are calculated before the therapy. The 3-D real shape of tumor necrosis core and MNPs distributed periphery would be formed by CT reconstructional technique. The positive change between MNPs concentration in the periphery and temperature increase in the whole tumor tissue would be computed. Only the narrow range of MNPs mass can produce the clinically acquired thermal dose. Thus, the thermal simulation for AEH should be more accurate.

Since the present models are not considering the two inhomogeneous factors simultaneously, we established a model to demonstrate temperature increase based on the analysis of heterogeneous interior heat source during AEH therapy. As tumors have various cores and peripheries which are reconstructed in favor of CT, we only modeled the tumor shape as a cuboid and the core as a sphere in order to show the character of temperature increase during AEH. Moreover, we compared the simulated results with the other two types of models at present stage to show the significant difference. For describing clearly, we define both SAR and MNPs homogeneously distributed model as SAR(++)&MNP(++), the SAR heterogeneously and MNPs uniformly distributed model as $\mathrm{SAR}(--)\&\mathrm{MNP}(++)$, the new model we established as $\mathrm{SAR}(--)\&\mathrm{MNP}(--)$.

In the study, the heating area is prescribed as in

$$\begin{aligned}\Omega \subseteq\ & [x = 1.5\ \mathrm{cm}, 0 \le y \le 3\ \mathrm{cm}, 0 \le z \le 2\ \mathrm{cm}]\\ \cup\ & [y = 1.5\ \mathrm{cm}, 0 \le x \le 3\ \mathrm{cm}, 0 \le z \le 2\ \mathrm{cm}]\\ \cup\ & [z = 1\ \mathrm{cm}, 0 \le x \le 3\ \mathrm{cm}, 0 \le y \le 3\ \mathrm{cm}]\end{aligned}$$

and the typical values for the tissue thermal properties are applied as given in [7], [23], [24], [38]

$$\begin{aligned}&\rho = 1020\ \mathrm{kg/m^3}, C = 3800\ \mathrm{J/kg\cdot K},\\ &K = 0.561\ \mathrm{W/m\cdot K}, h = 20\ \mathrm{W/m^2\cdot K}.\end{aligned}$$

In the tumor core $\omega_b = 0$ and in the periphery $\omega_b = 0.515$ kg/m·s.

Brunke *et al.* [36] are using the synchrotron radiation based micro-computed tomography (SR μCT) to investigate 3-D MNPs concentration distribution in the tissues. Because of the

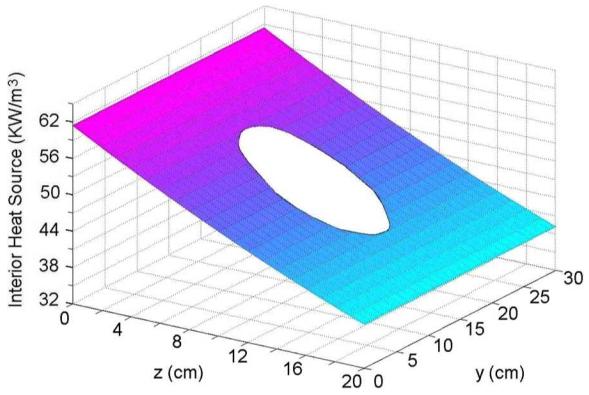

Fig. 5. The 3-D graph of inhomogeneous interior heat source analyzed on x–z plane in the $\mathrm{SAR}(--)\&\mathrm{MNP}(--)$ model.

lack of sufficient experimental data at present, we set particle concentration in the model as some disperse constants in the periphery. The algorithm to the BHT equation was referred to Lv [24]. In this paper, we calculated in favor of the software Fluent 6.2.

III. Results

A. 3-D Interior-Heat-Source Distribution

Fig. 5 shows the IIA analyzed 3-D interior-heat-source distribution on the x–z plane in the tumor model. The SAR values in the model were detected in the *in vitro* material experiment. The MNPs SAR values which were detected from the MNPs-gelled sample were the same in the $\mathrm{SAR}(++)\&\mathrm{MNP}(--)$ as $\mathrm{SAR}(--)\&\mathrm{MNP}(++)$model. We scaled the MNPs SAR values to make the total SAR generated in the new model equal to the total SAR generated in the above two models.

The temperature increase in the tumor is dose-dependent when the external ac magnetic field is stable. We simulated various MNPs concentration in the periphery which produced different thermal field in the tumor. Based on the results, we can obtain the appropriate MNPs doses for effective thermal therapy clinically.

B. Characteristic of Temperature Elevation

In the experiments of temperature detecting in rabbit VX-2 liver tumor, the typical heating curve obtained by Moroz, etc., showed that the tumor periphery was maintained higher temperature than the tumor core for the necrosis areas [2], [3], [6]. This phenomenon can be explained by the theoretical model established. Fig. 7 shows that at the initial heating, the tumor center maintained lower temperature as result of being devoid of MNPs. The SAR value in the center is zero. The temperature rise in the area only depended on the heat transfer from the adjacent tumor periphery. Beside the tumor core, temperature distribution is inhomogeneous within the tumor rim due to the SAR distribution. The attenuation of ac magnetic field exists in the aperture of the ferrite-core applicator, which leads to the heterogeneity of SAR values. The experiment showed that the attenuation mainly focused on the z direction while much slighter on x and y directions. Thus, we can merely consider the SAR value as function of z coordinate, making the calculation simplified.

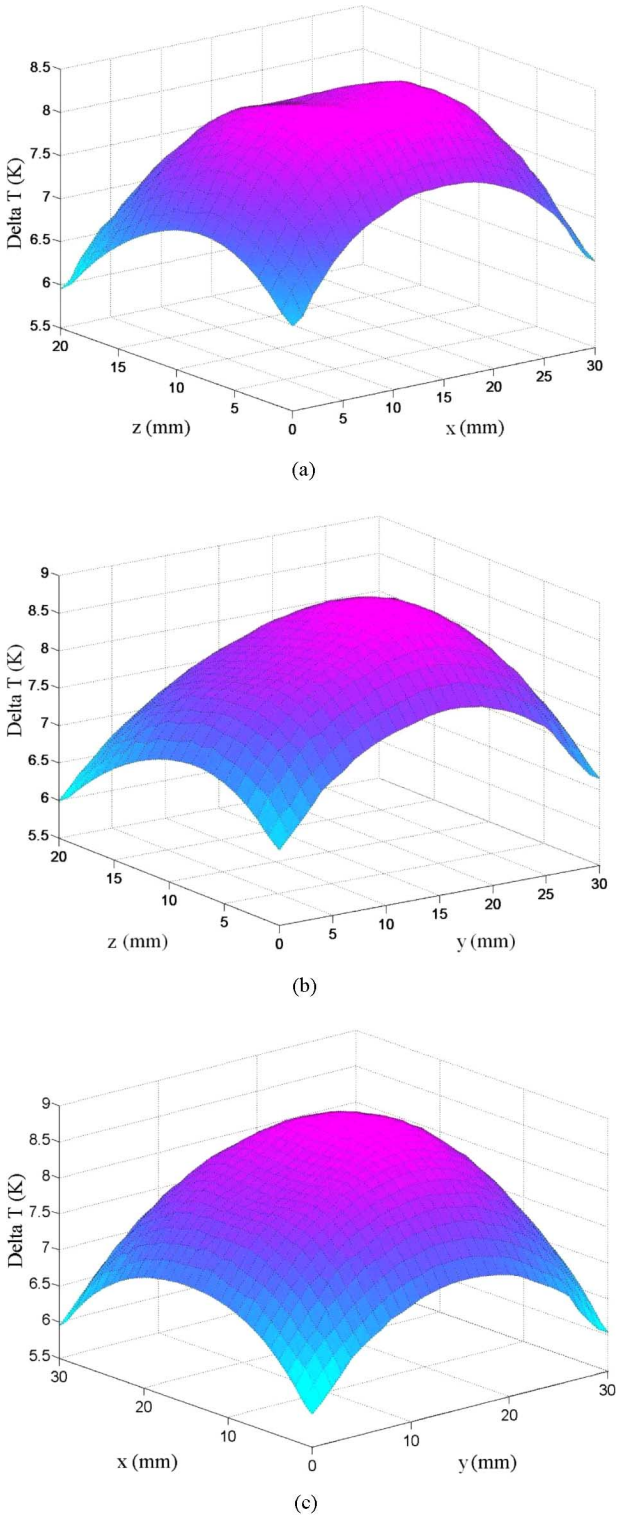

Fig. 6. 3-D graphs of temperature elevation after 40 min heating at (a) x-z, (b) y-z, and (c) x-y planes.

After more than 40 min of heating, temperature in the tumor reaches nearly in a steady state. The maximum and minimum points occur within the tumor rim, not in the tumor center.

In virtual of the much slighter attenuation of magnetic field on x and y directions and little MNPs depositing in the tumor center, the difference between the maximum with minimum

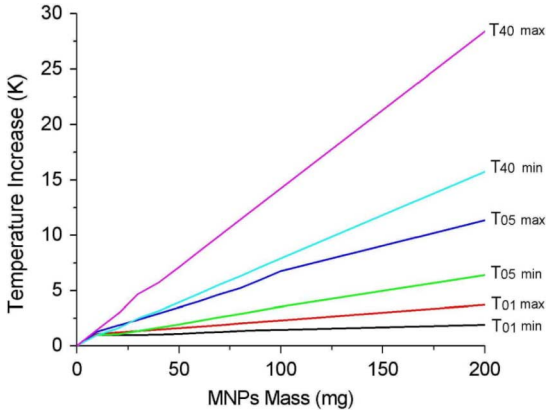

Fig. 7. Typical curves in the phantom at maximum and minimum spot, respectively, at 1 (T_{01}), 5 (T_{05}), and 40 (T_{40}) min.

temperature is smaller in contrast with the heat generated by external electrodes, microwaves, or ultrasound (see Fig. 6).

There was a positive relationship between tumor MNPs concentration and heating rate in the rabbit experiments [3]. Fig. 7 shows the simulated results in the model that different masses of MNPs in the tumors resulted in the proportional temperature rise. Keeping the external ac magnetic field, the maximum and minimum temperature can be maintained as clinical requirement by regulating of the mass of MNPs in the tumor.

Fig. 8 shows the significant difference in thermal distribution at the x-z plan after 1 and 40 min heating in the $\mathrm{SAR}(--)\&\mathrm{MNP}(--)$ with $\mathrm{SAR}(--)\&\mathrm{MNP}(++)$ model. The significant difference temperature distribution among the two models indicated that MNPs distribution in the tumors mainly determined the thermal distribution in the tissues.

Fig. 9 shows the significant different values of increased temperature as function of MNPs mass in the $\mathrm{SAR}(--)\&\mathrm{MNP}(--)$ and $\mathrm{SAR}(++)\&\mathrm{MNP}(++)$ model after 40 min heating at maximum and minimum spots, respectively. The significant different values of temperature elevation among the two models indicated that 3-D SAR spatial distribution mainly affected the precision of simulation results and IIA is preferable when accurate HTP are required during AEH.

IV. Discussion and Conclusion

Hyperthermia treatment planning will ultimately provide information about the actual temperature distributions obtained and thus the tumor control probability (TCP) is to be expected [22]. Thermal simulation will improve the understanding of the present clinical results of thermotherapy and will greatly help both in optimizing clinical heating technology and in designing optimal clinical trials.

During AEH treatment temperature distribution is inhomogeneous in the liver tumor. From the comparison of simulation between the $\mathrm{SAR}(--)\&\mathrm{MNP}(--)$ and $\mathrm{SAR}(--)\&\mathrm{MNP}(++)$ model, MNPs distribution in the tumors mainly determined the thermal distribution in the tissues. From the contrast of theoretical calculation between the $\mathrm{SAR}(--)\&\mathrm{MNP}(--)$ and SAR(++)&$\mathrm{MNP}(++)$ model, SAR spatial distribution mainly affected the precision of simulation results.

There is a significant linear relationship between the heating rate and MNP concentration. Thus, temperature can be regulated by quantity control of MNPs in the tumor, as well as by controlling the external ac magnetic field.

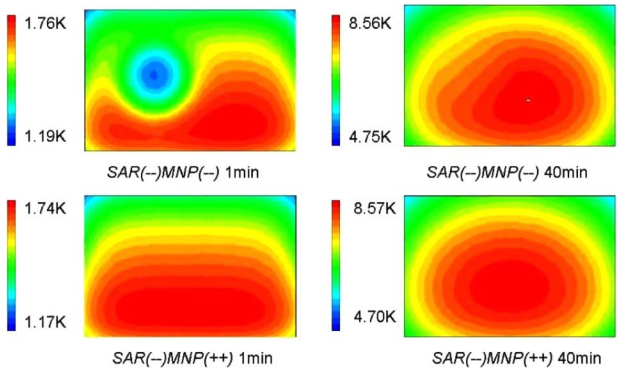

Fig. 8. The difference in thermal distribution at the x-z plan after 1 and 40 min heating in the $\mathrm{SAR}(--)\&\mathrm{MNP}(--)$ and $\mathrm{SAR}(--)\&\mathrm{MNP}(++)$ model.

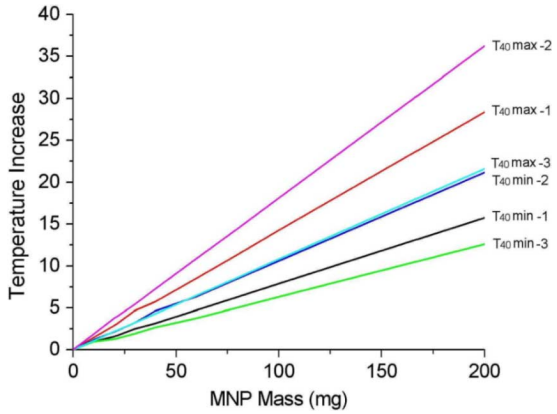

Fig. 9. The significant difference in increased temperature as function of MNPs mass in the $\mathrm{SAR}(--)\&\mathrm{MNP}(--)$ and SAR(++)&$\mathrm{MNP}(++)$ model after 40 min heating at maximum and minimum spots, respectively. The temperature elevation curves in the $\mathrm{SAR}(--)\&\mathrm{MNP}(--)$ model were labeled $T_{40}\max -1$ and $T_{40}\min -1$. In the SAR(++)&$\mathrm{MNP}(++)$ model, the maximum SAR producing temperature elevation curves were named $T_{40}\max -2$ and $T_{40}\min -2$, the minimum $T_{40}\max -3$ and $T_{40}\min -3$.

Our further study will concentrate on the AEH treatment plan. Many factors that affect the accuracy of the simulation will be considered and the data of temperature detected in animal experiments will be accumulated for collecting statistic to compare with the theoretical results. Thus, the computer-aided simulation will deeply impact on the clinical therapy of patients in the future.

Acknowledgment

This work was supported by 973 Project of China (No. 2006CB933206), National Fund (No. 30470507), and the Scientific Research Foundation of Graduate School of Southeast University.

References

[1] M. Mitsumori, M. Hiraoka, T. Shibata, Y. Okuno, Y. Nagata, Y. Nishimura, M. Abe, M. Hasegawa, H. Nagae, and Y. Ebisawa, "Targeted hyperthermia using dextran magnetite complex: A new treatment modality for liver tumors," *Hepatogastroenterology*, vol. 43, pp. 1431–1437, 1996.

[2] T. Minamimura, H. Sato, S. Kasaoka, T. Saito, S. Ishizawa, S. Takemori, K. Tazawa, and K. Tsukada, "Tumor regression by inductive hyperthermia combined with hepatic embolization using dextran magnetite incorporated microspheres in rats," *Int. J. Oncology*, vol. 16, pp. 1153–1158, 2000.

[3] P. Moroz, S. K. Jones, J. Winter, and B. N. Gray, "Targeting liver tumors with hyperthermia: Ferromagnetic embolization in a rabbit liver tumor model," *J. Surg. Oncol.*, vol. 78, pp. 22–29, 2001.

[4] P. Moroz, S. K. Jones, and B. N. Gray, "Tumor response to arterial embolization hyperthermia and direct injection hyperthermia in a rabbit liver tumor model," *J. Surg. Oncol.*, vol. 80, pp. 149–156, 2002.

[5] P. Moroz, H. Pardoe, S. K. Jones, T. G. S. Pierre, S. Song, and B. N. Gray, "Arterial embolization hyperthermia: Hepatic iron particle distribution and its potential determination by magnetic resonance imaging," *Phys. Med. Biol.*, vol. 47, pp. 1591–1602, 2002.

[6] S. K. Jones, J. Winter, and B. N. Gray, "Treatment of experimental rabbit liver tumours by selectively targeted hyperthermia," *Int. J. Hyperther.*, vol. 18, pp. 117–128, 2002.

[7] R. Z. Xu, Y. Zhang, M. Ma, J. G. Xia, J. W. Liu, Q. Z. Guo, and N. Gu, "Measurement of specific absorption rate and thermal simulation for arterial embolization hyperthermia in the maghemite-gelled model," *IEEE Trans. Magn.*, vol. 43, no. 3, pp. 1078–1085, Mar. 2007.

[8] A. Jordan, R. Scholz, P. Wust, H. Fähling, and R. Felix, "Magnetic fluid hyperthermia (MFH): Cancer treatment with AC magnetic field induced excitation of biocompatible superparamagnetic nanoparticles," *J. Magn. Magn. Mater.*, vol. 201, pp. 413–419, 1999.

[9] A. Jordan, R. Scholz, K. Maier-Hauff, M. Johannsen, P. Wust, J. Nadobny, H. Schirra, H. Schmidt, S. Deger, S. Loening, W. Lanksch, and R. Felix, "Presentation of a new magnetic field therapy system for the treatment of human solid tumors with magnetic fluid hyperthermia," *J. Magn. Magn. Mater.*, vol. 225, pp. 118–126, 2001.

[10] M. Babincová, V. Altanerrová, Č. Altaner, P. Čičmanec, and P. Babinec, "In vivo heating of magnetic nanoparticles in alternating magnetic field," *Med. Phys.*, vol. 31, pp. 2219–2221, 2004.

[11] M. Johannsen, U. Gneveckow, L. Eckelt, A. Feussner, N. WaldÖFner, R. Scholz, S. Deger, P. Wust, S. A. Loening, and A. Jordan, "Clinical hyperthermia of prostate cancer using magnetic nanoparticles: Presentation of a new interstitial technique," *Int. J. Hyperther.*, vol. 21, pp. 637–647, 2005.

[12] K. Maier-Hauff, R. Rothe, R. Scholz, U. Gneveckow, P. Wust, B. Thiesen, A. Feussner, A. Deimling, N. Waldoefner, R. Felix, and A. Jordan, "Intracranial thermotherapy using magnetic nanoparticles combined with external beam radiotherapy: Results of a feasibility study on patients with glioblastoma multiforme," *J. Neurooncol.*, vol. 82, pp. 53–60, 2007.

[13] C. Breedis and G. Young, "The blood supply of neoplasms in the liver," *Amer. J. Pathol.*, vol. 30, pp. 969–985, 1954.

[14] K. V. Stribley, B. N. Gray, R. L. Chmiel, J. C. P. Heggie, and R. C. Bennett, "Internal radiotherapy for hepatic metastases; The blood supply of hepatic metastases," *Surg. Res.*, vol. 33, pp. 25–32, 1982.

[15] S. Archer and B. N. Gray, "The vascularization of small liver metastases," *Br. J. Surg.*, vol. 76, pp. 545–548, 1989.

[16] S. Archer and B. N. Gray, "Comparison of portal vein chemotherapy with hepatic arterial chemotherapy in the treatment of liver micrometastases," *Amer. J. Surg.*, vol. 159, pp. 325–329, 1990.

[17] M. A. Burton, B. N. Gray, P. F. Klemp, D. K. Kelleher, and N. Hardy, "Selective internal radiation therapy: Distribution of radiation in the liver," *Eur. J. Cancer Clin. Oncol.*, vol. 25, pp. 1487–1491, 1989.

[18] S. Ho, W. Y. Lau, T. W. Leung, and P. J. Johnson, "Internal radiation therapy for patients with primary or metastatic hepatic cancer: A review," *Cancer*, vol. 83, pp. 1894–1907, 1998.

[19] N. Kemeny, Y. Huang, A. M. Cohen, W. Shi, J. A. Conti, M. F. Brennan, J. R. Bertino, A. D. M. Turnbull, D. Sullivan, J. Stockman, L. H. Blumgart, and Y. Fong, "Hepatic arterial infusion of chemotherapy after resection of hepatic metastases from colorectal cancer," *New. Engl. J. Med.*, vol. 341, pp. 2039–2048, 1999.

[20] A. M. Campbell, I. H. Bailey, and M. A. Burton, "Analysis of the distribution of intra-arterial microspheres in human liver following hepatic yttrium-90 microsphere therapy," *Phys. Med. Biol.*, vol. 45, pp. 1023–1033, 2000.

[21] R. S. J. P. Kaatee, H. Grezee, and A. G. Visser, "Temperature measurement errors with thermocouples inside 27 MHz current source insterstitial hyperthermia applicators," *Phys. Med. Biol.*, vol. 44, pp. 1499–1511, 1999.

[22] J. J. W. Lagendijk, "Hyperthermia treatment planning," *Phys. Med. Biol.*, vol. 45, pp. R61–R76, 2000.

[23] N. Tsafnat, G. Tsafnat, T. D. Lambert, and S. K. Jones, "Modelling heating of liver tumours with heterogeneous magnetic microsphere deposition," *J. Phys. Med. Biol.*, vol. 50, pp. 2937–2953, 2005.

[24] Y. Lv, Z. Deng, and J. Liu, "3-D numerical study on the induced heating effects of embedded micro/nanoparticles on human body subject to external medical electromagnetic field," *IEEE Trans. Nanobiosci.*, vol. 4, no. 4, pp. 284–294, Dec. 2005.

[25] W. Andra, C. G. Ambiy, R. Hergt, I. Hilger, and W. A. Kaiser, "Temperature distribution as function of time around a small spherical heat source of local magnetic hyperthermia," *J. Magn. Magn. Mater.*, vol. 194, pp. 197–203, 1999.

[26] A. M. Granov, O. V. Muratov, and V. F. Frolov, "Problems in the local hyperthermia of inductively heated embolized tissues," *J. Theor. Found. Chem. Eng.*, vol. 36, pp. 63–66, 2002.

[27] S. Maenosono and S. Saita, "Theoretical assessment of FePt nanoparticles as heating elements for magnetic hyperthermia," *IEEE Trans. Magn.*, vol. 42, no. 6, pp. 1638–1642, Jun. 2006.

[28] U. Gneveckow, A. Jordan, R. Scholz, V. Brüß, N. Waldöfner, J. Ricke, A. Feussner, B. Hildebrandt, B. Rau, and P. Wust, "Description and characterization of the novel hyperthermia and thermoabation-system MFH® 300 F for clinical magnetic fluid hyperthermia," *Med. Phys.*, vol. 31, pp. 1444–1451, 2004.

[29] P. L. Roberson, R. K. T. Haken, D. L. McShan, P. E. McKeever, and W. D. Ensminger, "Three-dimensional tumor dosimetry for hepatic yttrium-90-microsphere therapy," *J. Nucl. Med.*, vol. 33, pp. 735–738, 1992.

[30] A. M. Campbell, I. H. Bailey, and M. A. Burton, "Analysis of the distribution of intra-arterial microspheres in human liver following hepatic yttrium-90 microsphere therapy," *Phys. Med. Biol.*, vol. 45, pp. 1023–1033, 2000.

[31] S. H. Sun, H. Zeng, D. B. Robinson, S. Raoux, P. M. Rice, S. X. Wang, and G. X. Li, "Monodisperse MFe_2O_4(M) Fe, Co, Mn) nanoparticles," *J. Amer. Chem. Soc.*, vol. 124, pp. 273–279, 2002.

[32] T. Hyeon, S. S. Lee, J. Park, Y. Chung, and H. B. Na, "Synthesis of highly crystalline and monodisperse maghemite nanocrystallites without a size-selection process," *J. Amer. Chem. Soc.*, vol. 123, pp. 12798–12801, 2001.

[33] N. R. Jana, Y. F. Chen, and X. G. Peng, "Size- and shape-controlled magnetic (Cr, Mn, Fe, Co, Ni) oxide nanocrystals via a simple and general approach," *Chem. Mater.*, vol. 16, pp. 3931–3935, 2004.

[34] J. Park, K. An, Y. Hwang, J. G. Park, H. J. Noh, J. Y. Kim, J. H. Park, N. M. Hwang, and T. Hyeon, "Ultra-large-scale syntheses of monodisperse nanocrystals," *Nature Mater.*, vol. 3, pp. 891–895, 2004.

[35] L. M. Bronstein, X. L. Huang, J. Retrum, A. Schmucker, M. Pink, B. D. Stein, and B. Dragnea, "Influence of iron oleate complex structure on iron oxide nanoparticle formation," *Chem. Mater.*, vol. 19, pp. 3624–3632, 2007.

[36] O. Brunke, S. Odenbach, R. J. C. Alexiou, I. Hilger, and F. Beckmann, "Determination of the magnetic particle distribution in tumour tissue by means of X-ray tomography," *Phys. Condens. Mater.*, vol. 18, pp. 2903–2917, 2006.

[37] H. H. Pennes, "Analysis of tissue and arterial temperature in the resting human forearm," *J. Appl. Physiol.*, vol. 1, pp. 93–122, 1948.

[38] M. M. Chen, K. R. Holmes, and V. Rupinskas, "Pulse-decay method for measuring the thermal conductivity of living tissues," *ASME J. Biomech. Eng.*, vol. 103, pp. 253–260, 1981.

[39] S. Weinbaum, L. M. Jiji, and D. E. Lemona, "Theory and experiment for the effect of vascular microstructure on surface tissue heat transfer—Part I: Anatomical foundation and model conceptualization," *ASME J. Biomech. Eng.*, vol. 106, pp. 321–320, 1986.

[40] R. E. Rosensweig, "Heating magnetic fluid with alternating magnetic field," *J. Magn. Magn. Mater.*, vol. 252, pp. 370–374, 2002.

[41] Q. A. Pankhurst, J. Connolly, S. K. Jones, and J. Dobson, "Application of magnetic nanoparticles in biomedicine," *J. Phys. D: Appl. Phys.*, vol. 36, pp. 167–181, 2003.

[42] M. Ma, Y. Wu, J. Zhou, Y. K. Sun, Y. Zhang, and N. Gu, "Size dependence of specific power absorption of Fe_3O_4 particles in AC magnetic field," *J. Magn. Magn. Mater.*, vol. 268, pp. 33–39, 2004.

[43] P. Liang, B. W. Dong, X. L. Yu, D. J. Yu, Z. G. Cheng, L. Su, J. S. Peng, Q. Nan, and H. J. Wang, "Computer-aided dynamic simulation of microwave-induced thermal distribution in coagulation of liver cancer," *IEEE Trans. Biomed. Eng.*, vol. 48, pp. 821–829, 2001.